UNIVERSITA' CAMPUS BIO-MEDICO DI ROMA
UNIVERSITA' DEGLI STUDI DI ROMA "TOR VERGATA"

Master Universitario congiunto di II livello in
"Radioprotezione: Sicurezza nel campo delle Radiazioni Ionizzanti e Radiazioni Non Ionizzanti"

Titolo:

Physics meets Surgery – Radiation-protection issues and solutions in hybrid operating rooms

Relatore
Ing. Aldo Delia

Candidata
Dott. Alexandra Parmentier

Correlatore
Ing. Marco Martellucci

2016-2018

Physics meets Surgery

Radiation-protection issues and solutions in hybrid operating rooms

ALEXANDRA PARMENTIER

Level-II Master Program in Radiation Protection - 2^{nd} Edition
University of Rome Tor Vergata $\&$ Campus Bio-Medico University of Rome

PHYSICS MEETS SURGERY
Radiation-protection issues and solutions in hybrid operating rooms

SUPERVISORS
A. Delia, M. Eng., Scientific Coordinator of the Master Program
M. Martellucci, M. Eng, Scientific Coordinator of the Master Program

MASTER DIRECTORS
Prof. R. Senesi, Dept. of Physics, Univ. of Rome Tor Vergata, Italy
Prof. S. Silvestri, Dept. of Biomedical Engineering, Campus Bio-Medico Univ. of Rome, Italy

Master Thesis 2016-2018
University of Rome Tor Vergata
Campus Bio-Medico University of Rome Rome, Italy

Cover: A hybrid operating room equipped with Siemens Imaging Systems.
By J.M. Keckler Medical Co., Inc. (U.S.A.).

Typeset in LaTeX
Rome, Italy 2018

Abstract

The present level-II Master thesis stems from 18 months of attendance of a specialized post-graduate course in Radiation Protection at the University of Rome Tor Vergata and Campus Bio-Medico University of Rome, Italy.
This effort was accompanied by the participation in a six-month training course organized by Policlinico Tor Vergata (Rome, Italy) in order to earn the necessary credits to apply for the national examination as a 1^{st}-grade Qualified Expert in ionizing radiation.
The layout of the monograph has been thought for a broad audience, and aims at describing major radiation-protection issues occurring in hybrid operating rooms (HORs) when X-ray imaging devices are in use, as well as typical solutions implemented by experts involved in site planning.
After a brief introduction on the why and how of HORs, Chapter 2 synthetically describes the functioning of X-ray devices of common use in HORs, while Chapter 3 offers a scheme of major fluoroscopic dose metrics, and Chapter 4 reports details of a 2017 Spanish radiation-protection study on an actual HOR recently inaugurated at the Hospital Clínico Universitario de Valladolid.
A set of conclusions and an appendix on major features of X-ray tubes complete the document.

Keywords: hybrid operating rooms, X-ray imaging, radiation dosimetry, site planning

Contents

List of Figures

List of Tables

1
Introduction

1.1 Going hybrid

The hybrid operating room (HOR) is an interesting concept, marrying two areas - namely, radiological imaging and surgery - characterized by distinct problems and concerns.
Imaging has a long history in the operating room (OR). Since the late 1960s mobile C arms (*i.e.*, portable fluoroscopic systems) have become a mainstay of modern ORs; yet, increasingly complex surgical and interventional approaches have led larger facilities to switch to a HOR configuration in order to combine sterile surgical equipment for open procedures with a fixed, integrated imaging system, which allows to overcome many typical limitations of conventional theaters.
Reasonably, it has been the rapid growth of minimally invasive surgery (MIS) to boost the general interest in HORs, due to the crucial possibility of intra- and postoperative on-table imaging and intervention.

1.2 Clinical applications

The HOR is designed to be extremely versatile, since it allows for a variety of open surgical, laparoscopic, interventional radiological, and hybrid procedures to be performed. In addition, the usual large size of the work environment, the high-resolution imaging instrumentation, and the manoeuvrable operating table make this kind of theater suitable for developments in robot-assisted surgery.
Fig. 1.1 and Table 1.1 show an outline of the multidisciplinary usage of HORs, as reported by surgeons of the Broomfield Hospital of Chelmsford, UK [1]. From these data, one can evince how effectively HORs enable physicians to perform the most advanced vascular and surgical procedures with a high level of sterility and unrestricted imaging.
On the other hand, though the benefits of interventional radiology are beyond dispute, the complexity of these procedures, in terms of both large medical staff involved and work frequency, leads to relatively high occupational radiological exposures [2], as well as higher exposures to patients [3, 4], when compared to conventional practices.

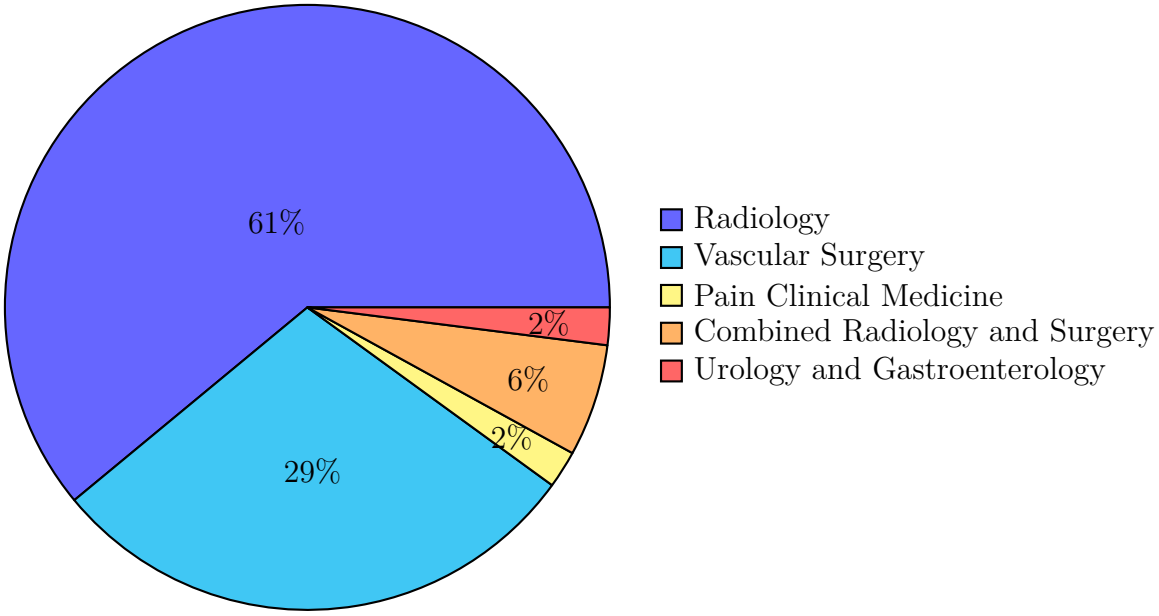

Figure 1.1: Pie chart summarizing the multi-specialty usage of a HOR. Adapted from [1].

For this reason, the importance of this topic has been reviewed by the board of the Cardiovascular and Interventional Radiological Society of Europe (CIRSE), which has recently created and implemented dedicated guidelines in cooperation with the American Society of Interventional Radiology (SIR) [5, 6].

Table 1.1: Summary of typical clinical activities performed in HORs at the Broomfield Hospital of Chelmsford, UK, which outlines the extremely versatile nature of the hybrid theatre. Adapted from [1].

	Activities
Endovascular	angiogram - thrombolysis - angioplasty - venogram
Interventional radiology	mesenteric/renal/splenic artery/varicocele embolization - ureteric stent insertion - fistulogram - nephrostomy
Open vascular surgery	open AAA repair - axillary/bifemoral bypass - femoral/popliteal bypass - femoral/femoral X over - carotid endarterectomy - knee amputation - SFJ ligation, stripping of LSV+ avulsions - wound debridement and SSG - wedge toe nail excision - lymph node biopsy - transaxillary division of subclavius - diagnostic laparoscopy - laparoscopic inguinal hernia repair - endovenous laser ablation of varicose veins - robot assisted laparoscopic repair of type II endoleak
Hybrid procedures	EVAR - EVAR and simultaneous embolisation of IIA - repair of type 1 endoleak - femoral endarterectomy/on table angioplasty - SFA angioplasty and transmetatarsal amputation
Emergency	angiogram and axillary embolectomy - aorto biiliac/bifemoral bypass/on table angiogram - angioplasty, emergency cut down to CFA and thrombectomy - venous thrombectomy, on-table venogram and venoplasty
Other	Hickman line insertion - Portacath insertion - ERCP/PTC - OGD - facet joint injections - PCNL - oesophageal stenting

2

X-ray imaging techniques in the HOR

2.1 Image-guided therapy

Image-guided therapy (IGT), a central concept of modern medicine, is a multi-modality discipline that aims to use any form of medical imaging to improve the localization and targeting of diseased tissues, as well as to monitor and control treatments [7].
Traditional surgery makes use of hand–eye coordination; for this reason, it shows limitations due to the inadequacies of human visualization and dexterity.
On the one hand, the surgeon operates within a 3D volume, which includes the targeted tissue and its related anatomy. Such a volume is not directly visible because electromagnetic (e.m.) radiation in the visible range cannot penetrate the skin or exposed surfaces[1]. In addition, the recognition of tumor margins is often a hard task for the physician, which causes intraoperative decision making to be extremely difficult.
On the other hand, for the interventional radiologist similar limitations exist because percutaneous procedures, as well as the monitoring of functional parameters such as tissue perfusion, are not directly available to the human eye.
IGT is the answer to the above issues.
IGT currently employed in HORs mainly relies on X-ray based, magnetic-resonance (MR) based, and ultrasound techniques. The first family is the one of interest here.

2.2 Major techniques

2.2.1 The CT principle

During the 1970s, computed tomography (CT) represented an enormous step towards diagnostic advance in medicine, being the first method to non-invasively acquire images of the inside of the human body that were not biased by superposition

[1]Under normal conditions, light impinging on the skin surface (or most of exposed tissues) undergoes reflection, refraction, diffraction and absorption.

If the skin is dry, and possibly scaly, most of this light is reflected off the *stratum corneum* (the outest layer of the epidermis), whose refractive index is larger compared to that of air. This "surface glare"overwhelms the retina of the observer, preventing him/her from visualizing visible rays reflected from deeper skin layers.

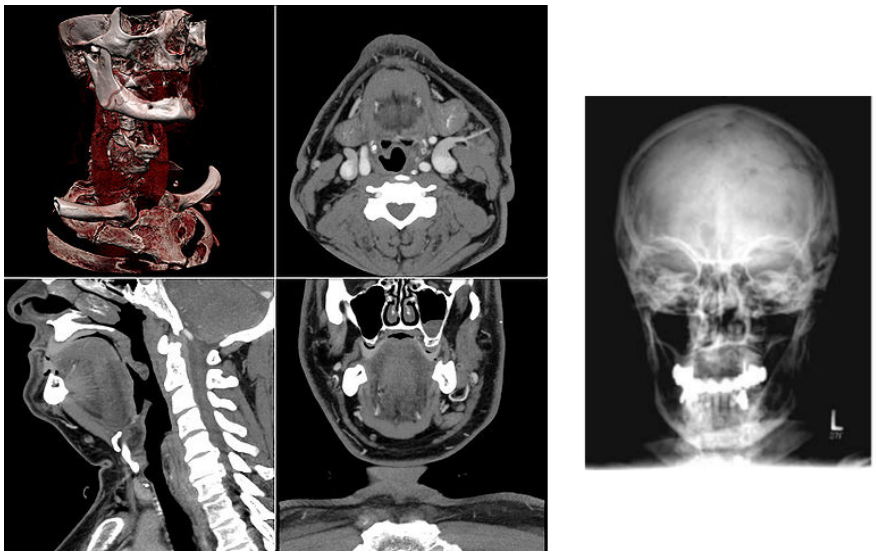

Figure 2.1: Left: CT of the head/neck area - volumetric reconstruction (top left), axial plane (top right), sagittal plane (bottom left), frontal plane (bottom right). By ChumpusRex Wikipedia user. Licensed under CC BY-SA 3.0 via Commons. Right: Conventional planar X-ray representation of the skull (reprinted from [8]). This image shows the high attenuation of X-rays within the cranial bone, while the small differences in attenuation that characterize soft tissue are not visible at all. The morphology of the brain is completely lost in the averaging process.

of distinct anatomical structures [8].

Conventional X-ray imaging suffers from the severe drawback that it only generates 2D projections of a 3D object[2]. This results in a reduction in spatial information (Fig. 2.1).

Historically, four different generations of CT have come in succession. Their classification is influenced by X-ray-tube and detector style, as well as the way they move around the patient.

The first generation refers to a rotate/translate geometry known as the "pencil beam"(Fig. 2.2, top left), in which an X-ray tube emits a single needle-like X-ray beam, which is selected from the X-ray cone by means of a pinhole collimator. On the opposite side, a single detector is moved synchronously along with the X-ray tube, in a linear displacement that is repeated for different projection angles over 180°. The amount of X-ray attenuation is measured by the detector and subsequently digitally recorded. For each "slice", the spatial distribution of the tissue-attenuation coefficients is retrieved by Radon transform[3].

The pencil-beam principle is not practiced any longer.

The CT scanners of the second generation had one X-ray source with narrow "fan-

[2]Projectional radiography is, by definition, the branch of medical imaging that produces 2D images by X-ray absorption.

[3]The Radon transform R is an integral transform that maps a function f, defined on an (x, y)-plane, into a function Rf defined on the 2D space of lines that serve as the integration domain of line integrals of f.

The Radon transform is a typical inverse problem.

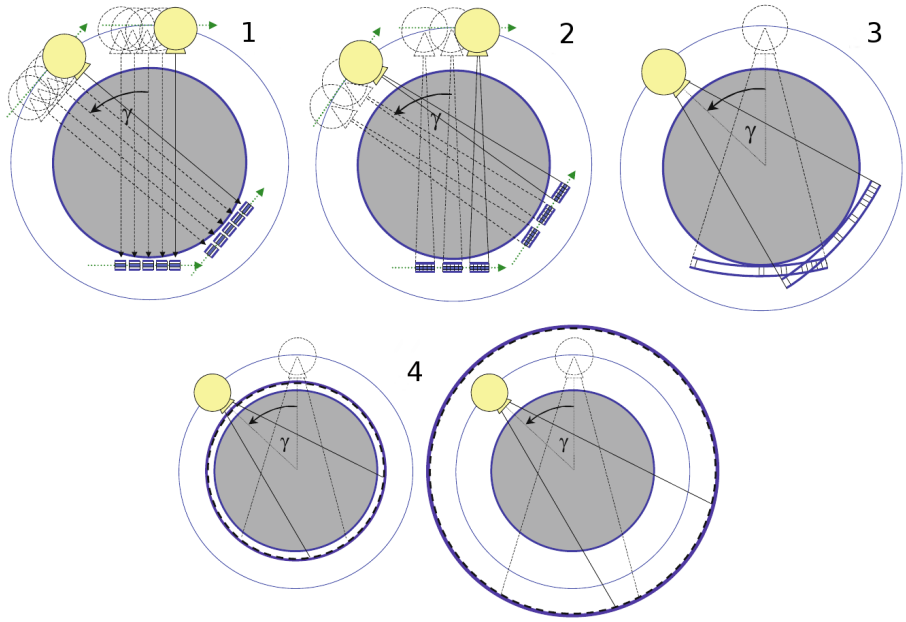

Figure 2.2: Top panel: pencil-beam scheme (top left), narrow fan-beam scheme (top center), and wide fan-beam scheme (top right). Bottom panel: fourth-generation scheme, with X-ray source either outside (bottom left) or inside (bottom right) the detector ring. Reprinted from [8].

beam", rotate/translate geometry (Fig. 2.2, top center), in which the X-ray fan was created from a conical X-ray source by means of a slit-shaped collimator. The detection device consisted of a short detector array including approximately 30 elements. Since the aperture angle of the fan beam was small (10° in the earliest devices), the X-ray tube and detector array still needed to be translated linearly before the projection angle was adjusted for another projection.

In comparison to the pencil-beam geometry, the acquisition time was reduced to a few minutes per slice, as the detector array was able to measure several intensities simultaneously. However, the measuring field was still small. For this reason, the second-generation scanners were still restricted, just like the first-generation homologues, to use in imaging of the cranium.

A major step towards achieving a significant reduction in acquisition time (less than 20 s) was an extension of the fan-beam concept, with the introduction of a larger fan angle and a correspondigly longer detector array (Fig. 2.2, top right). This gave origin to the third-generation of CT scanners, hosting wide fan beams between 40° and 60°, and detector arrays of 400-1000 elements, with no further need for linear displacement of the X-ray tube since the entire measuring field can be X-rayed simultaneously for one single projection angle (rotate/rotate geometry).

Fourth-generation scanners, developed in order to alleviate the ring artifacts produced by third-generation systems, have introduced no changes as to the X-ray tube. Instead, the difference resides in a closed, stationary detector ring (rotate/stationary geometry) with up to 5000 elements (Fig. 2.2, bottom panel), which can be internal or external with respect to the tube trajectory.

In case the detector ring is inside the tube trajectory, it is necessary to prevent the

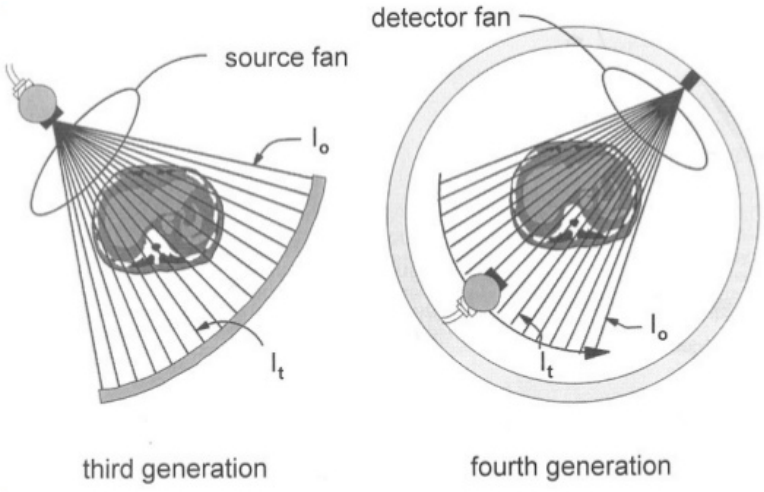

Figure 2.3: Left: fan beam in third-generation scanners. Right: inverse beam in fourth-generation scanners.

X-rays from radiating through the detectors from behind. For this reason, fourth-generation tomographs mount "inverse fans", which are centered on detectors rather than on the X-ray focus (Fig. 2.3).
Various other geometries, which have been developed and marketed in the last 20 years, do not precisely fit the above categories.
Electron-beam computed tomography (EBCT) has been developed since the 1980s for cardiac imaging [9]. Requiring very short acquisition times[4], this technique has indeed abandoned the concept of a localized X-ray tube rotating around the patient in favor of an electron beam focused onto tungsten target rings (Fig. 2.4), which are arranged in a half circle around the patient and quickly generate the desired X-ray fan beam upon impact with the electron beam, while the X-ray irradiation is measured with a stationary detector ring (stationary/stationary geometry).
The drawbacks reside in S/N ratio and spatial resolution, which are worse compared to conventional CT.
EBCT instrumentation represents the so-called fifth-generation family of CT tomographs.
In the 1990s, the introduction of the slip-ring technology (which enables spiral sampling) was identified as the sixth generation of CT scanners [11].
As the X-ray tube and detectors must be continuously supplied with energy, in older scanners the rate of circular movement was limited by the attachment of electric wires. This represented a massive obstacle to the reduction of acquisition time, since the X-ray sampling unit had to stop and start again after a certain angle of rotation.
In slip-ring technology, the energy is provided via sliding contacts situated between the gantry and the rotating sampling unit. This enables the sampling unit carrying

[4]Rapid imaging is important to prevent blurring of moving structures (such as the heart) during the scan.
Currently, the most advanced commercial designs can perform image sweeps in as little as 50 ms.

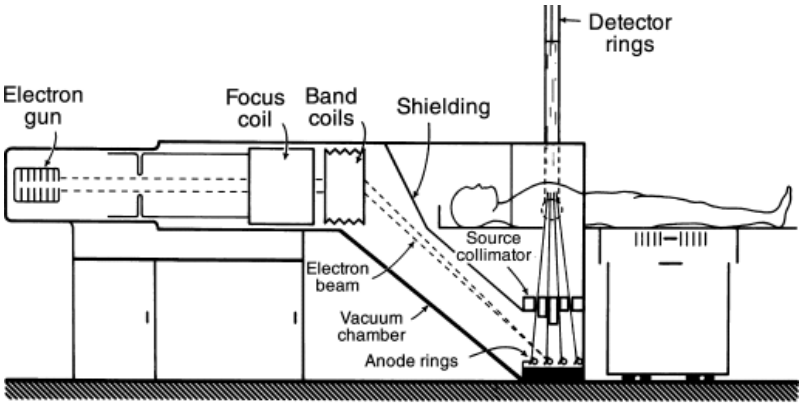

Figure 2.4: Scheme of a typical EBCT system. Reprinted from [10].

the X-ray source (and, in the case of third-generation scanners, the detector array) to rotate continuously.
The slip-ring innovation enabled a new acquisition technique: along with a continuous motion of the patient table through the sampling unit, it became possible to measure data in the shape of a spiral (helical geometry) [12].
The main drawback of helical CT scanners lies in data collection, since no full slices are available (no planar sections produced). This problem can be compensated for through the image reconstruction process.
Finally, C-arm tomographs consisting of a a flat-panel detector and a cone-shaped X-ray beam (cone-beam geometry) are referred to as the seventh generation (Fig. 2.5).
Unlike the pencil beam and fan beam, which are created by means of appropriate pin-hole or slit collimators re-shaping the original X-ray source intensity profile (with consequent efficiency reduction), the cone beam does not pass through a narrow collimator. Therefore, the initial X-ray beam can interact more efficiently and effectively with the detector, which causes the production of an outstanding amount of information in a very short time span. This poses technological challenges even today (especially in terms of the bandwidth needed for data transfer), and requires a much higher level of sophistication in the reconstruction process [8].

2.2.2 Fluoroscopy

X-ray fluoroscopy is probably the most commonly used method for image guidance in HORs.
Fluoroscopic procedures provide real-time projection images with high frame rates of several dozens images per second, a time resolution as short as a few ms, a spatial resolution on the order of several line pairs per mm, and fields of view as large as 30-40 cm [7].
After an early era[5] characterized by the introduction of the rotating anode to reach a compromise between high-quality imaging and the reduction of thermal damage

[5]Precisely, the decades immediately following Roentgen's 1895 discovery of X-rays by a Crookes discharge tube (see the Appendix).

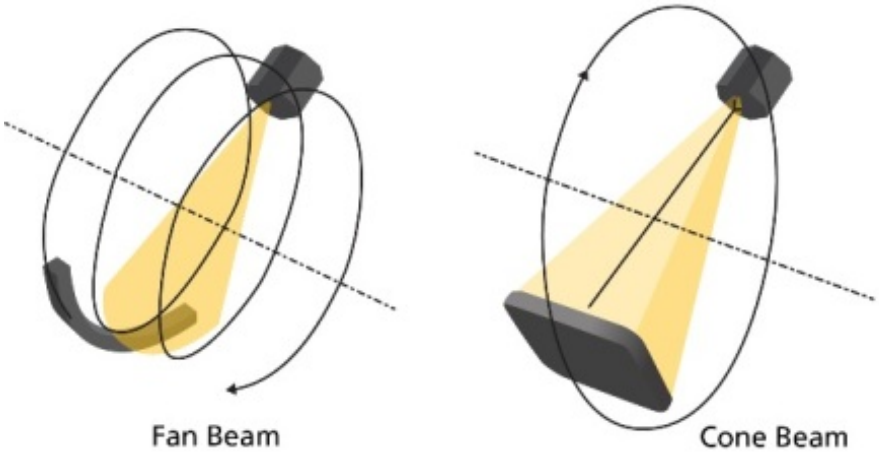

Figure 2.5: Major differences between cone-beam and fan-beam technologies. Reprinted from [13].

to the target, fluoroscopy was revolutionized by the advent, in the late 1940s and 1950s, of analog electronics, with the replacement of simple fluorescent screens - that is, scintillators with no secondary gain - by the X-ray image intensifier (XRII) in combination with optical-lense-coupled closed-circuit TV cameras (Fig. 2.6).
The XRII is a multi-stage vacuum tube suitable to convert X-ray photons into visible photons with large brightness gain in comparison to fluoroscopic screens (Fig. 2.6). A columnar cesium-iodide (CsI) input phospor performs the first conversion to visible photons, which get further converted to electrons by a coupled photocathode. Photoelectrons are then accelerated by a potential difference of 25-35 kV, and subsequently focused by electron lenses to the size of an output window, which is usually made of silver-activated zinc-cadmium sulphide able to convert photoelectrons into light again. Signal amplification (~ 5000) is obtained by photoelectron acceleration and "minification"of the photoelectron beam to the output-window size.
The XRII system represented a real breakthrough in fluoroscopic imaging, due to its effectiveness in enhancing the contrast performance and robustly cutting radiation dose down.
Digital electronics finally entered the fluoroscopic domain in the late 1960s, but it was only in the 1980s that enhanced video memory and computer technology, together with low-dose rapid switching X-ray tubes, brought the introduction of "pulsed fluoroscopy", which is able to trade off time resolution for lower dose. The 1990s witnessed the implementation of solid-state flat-panel detectors (FPDs, Fig. 2.7), which helped overcome image distorsions[6] and other disadvantages (non-linearity of light-intensity response, saturation, etc.) typical of XRII-TV chains.

[6]The input phosphor must be spherically configured to withstand the enormous external atmospheric pressure. Electrons accelerated from the curved photocathode to the planar output phosphor surface result in a peripheral image warping known as "pin-cushion distortion", causing relative errors of about 10% in distance measurements at the periphery.

Electrostatic and magnetic cylindrical focusing gradients tend to interact with surrounding magnetic fields, causing transient "S-distortions".

Vignetting (loss of light intensity at the periphery due to light-scattering phenomena) results in image non-uniformity.

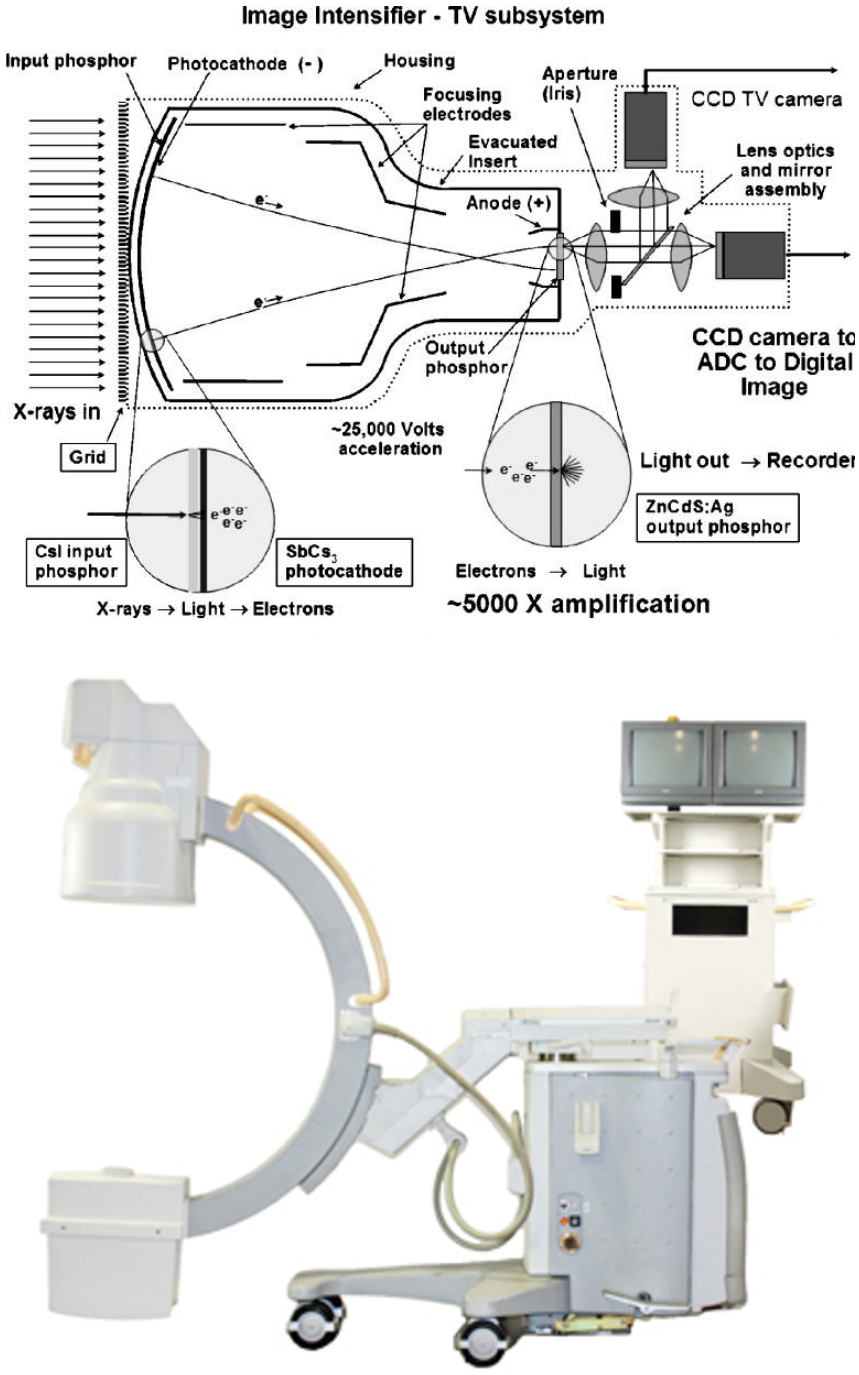

Figure 2.6: Top: Cross-sectional diagram of the XRII system (reprinted from [14]). Bottom: The Philips BV Pulsera mobile C-arm, mounting a 5-to-9 in (or 7-to-12 in) XRII.

Figure 2.7: A picture - taken during quality controls performed by personnel of Mardel s.r.l. in Feb 2018 - of one of the FPD fluoroscopy systems (fixed C arms) in use at Campus Bio-Medico University of Rome, Italy. A = X-ray tube; B = flat-panel image receptor.

In FPD systems the X rays directly impinge on the elements of an amorphous-silicon thin-film-transistor (a-Si TFT) array.
Each element of the array includes a TFT, a charge-collection electrode, and a storage capacitor (Fig. 2.8), all arranged on an a-Si substrate. Individual elements are connected by gate lines along rows (operating the TFT), drain lines along columns (connected to the TFT output), and charge amplifiers connected to the drain lines to receive the charge from specific detector elements (Fig. 2.8).
The TFT switch is kept closed during the exposure, so that incident X rays interact with the converter and produce a corresponding charge that is stored in the local capacitor. When the X-ray exposure is terminated, one gate line at a time is set high to activate all connected TFTs along the row, where the charge flows from the local capacitors through the transistors and down the drain lines in parallel to the output charge amplifiers at each column of the matrix. Digitization of the output signal occurs and the digital image is built up one row at a time. The deactivation of the gate line resets the TFTs for the next exposure, while the adjacent gate line is activated for the next row of data, with the process going on until the whole array is analyzed.
For continuous, real-time fluoroscopy (30 frames per second), all of the detector rows must be read in about 30 ms.
The TFT array and associated electronics are common to FPD systems, while X-ray detection and signal conversion can vary from system to system. Indirect detectors rely on a scintillator, which absorbs X-rays and produces light photons subsequently interacting with a photodiode electrode on the TFT array, in order to generate the corresponding charge in the element capacitor. Direct detectors use a semiconductor material sandwiched between two electrodes to absorb and convert the X-ray energy

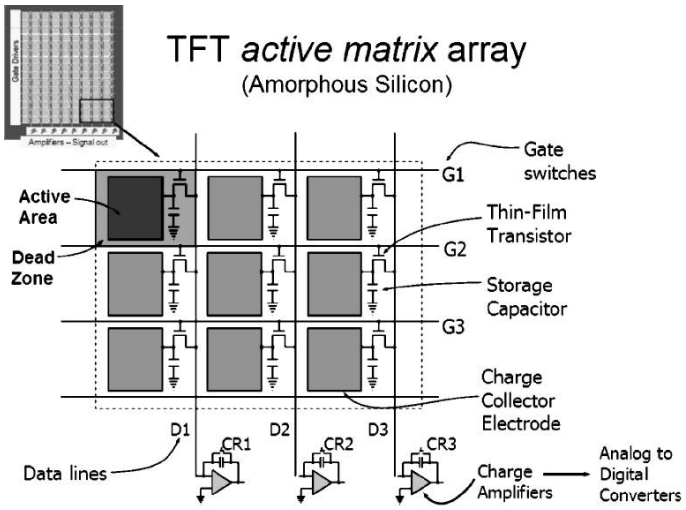

Figure 2.8: A scheme of an a-Si TFT. Reprinted from [14].

directly into ion pairs, with no photodiode needed, but just a charge-collection electrode.
Detective quantum efficiency (DQE), which is a measure of the detector's ability to preserve information in the image relative to the incident X-ray information presented at the phosphor, is usually higher for the FPD than for the XRII, except at the lowest exposures typically encountered in continuous fluoroscopy. Indeed, at high exposure levels (typical of radiography and digital subtraction angiography), the large signal produced by the absorbed X-rays calls for a low amplifier gain. Conversely, at fluoroscopy exposure levels, significant gain amplification is required to achieve a reasonable signal level for digitization, which results in an image with low signal-to-noise (S/N) ratio.

2.2.2.1 Rotational angiography

Fluoroscopy does not provide adequate depiction of cardiac anatomy or aneurysm phenomena in various organs, due to poor soft-tissue contrast and the 2D projective nature of the formed image, which hinders its application for complex procedures such as those involving catheter ablation.
A fix to this problem is provided by 3D rotational angiography[7] (3D RA), whose basic principle is similar to the CT scan, in which images acquired from different angles are reconstructed to a 3D image. A cone-beam geometry is usually implemented (CBCT).
The earliest technological implementation of RA made use of a standard fluoroscopy system consisting of an X-ray tube and an XRII mounted on a C-shaped gantry (C arm), which was rotated at 200° around the patient while acquiring X-ray projections at rates of 30-60 frames per second during continuous contrast agent injection [7]. In this system, the image distortions typical of the XRII required robust correction in

[7]Angiography is a medical imaging technique suitable to visualize the *lumen* of blood vessels and organs in the body by injection of a radio-opaque contrast agent, which enables imaging by X-ray based techniques such as fluoroscopy.

order to generate geometrically accurate 3D reconstructions of an object - a problem removed by the transition to the flat panel (Fig. 2.7).
Several of the steps in the reconstruction pipeline used to generate 3D volume images from a series of 2D projections are similar to those of clinical CT (Fig. 2.9).

2.2.2.2 Digital subtraction angiography

Digital subtraction angiography (DSA) is part of the larger phenomenon known as 2D subtraction radiography, whose purpose is to eliminate (or factor out) background complexity and amplify small differences by mutual subtraction of radiographic images that show contrast changes over time (temporal subtraction) or administration of X-ray intensity (energy subtraction).
In DSA, a contrast medium is injected intravenously; then X-ray detection before and after the injection is performed. After digitalization, the pre-contrast images are subtracted from those obtained after contrast administration so as to visualize arterial structures with no disturbance from superimposed bones and soft tissues.
The unparalleled resolution and clinical value of DSA has led to the use of intraoperative angiography to help guide the surgical management of several neurovascular conditions, also using portable C arms in the standard OR.

2.3 Image processing

2.3.1 Segmentation

Segmentation can be defined as the partition of an image into overlapping regions that are homogeneous with respect to image intensity or texture [7], with the aim of simplifying image representation into something easier to analyze.
During segmentation, a label is assigned to every image component (2D pixels or 3D voxels[8]) that shares specific characteristics, such as color, intensity, or texture. The result is a set of segments that collectively cover the entire image, or a set of extracted contour lines[9].
When applied to a stack of images, contours resulting from image segmentation can be used to create 3D reconstructions with the aid of interpolation algorithms.
The use of image segmentation is essential in IGT applications, especially in clinical settings. Indeed, in order to remove tumors or perform biopsies, surgeons must follow complex multiple trajectories to avoid critical anatomical structures. Before surgery, path planning and visualization is done using pre-operative 3D scans; during the procedure, the results of the pre-operative segmentation may still be used if the surgeon has access to the pre-operative planning information as 3D models and grayscale data are displayed in the OR. Also “on-the-fly”segmentation of real-time images generated during interventions can be used for quantitative monitoring of surgical progression.

[8] In computer graphics, a pixel is a point in a bitmap image, or, in general, the smallest addressable element in a display device. Its 3D counterpart is the voxel.

[9] A contour line, or equipotential curve, of a function of two variables is a curve along which the function has a constant value.

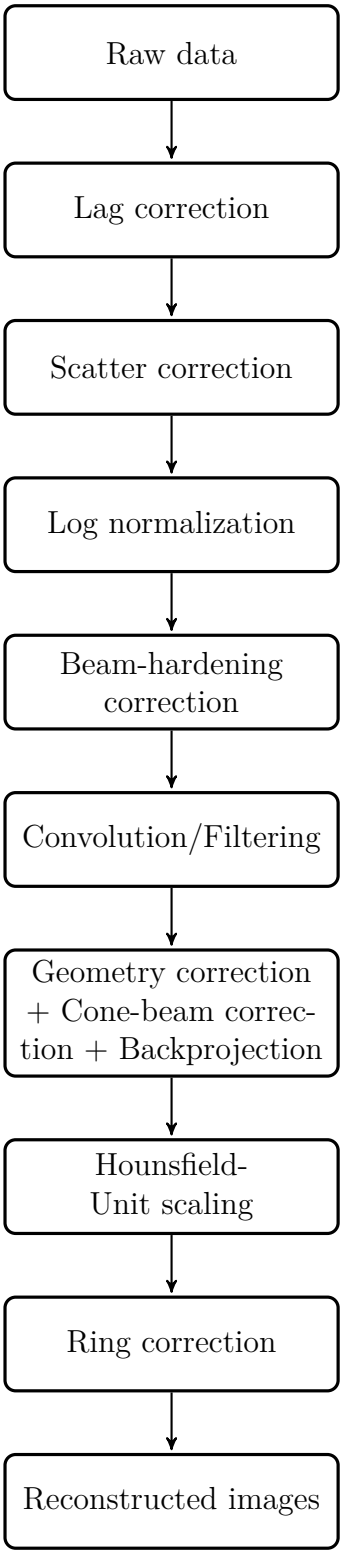

Figure 2.9: Flowchart of the reconstruction pipeline followed in rotational angiography to generate 3D volume images from a series of 2D projections. Several of the steps mimic those used in clinical CT, but some (such as geometry correction) are unique to the C-arm system implementing RA. Adapted from [7].

2.3.2 2D-3D registration

The registration of pre-operative 3D datasets to intra-operative 2D images can provide, in applications from orthopedics to neurosurgery, up-to-date information about patient position and location of medical instrumentation at the treatment site, thus aiding surgical guidance.
Pre-operative images provide an excellent source of detail about anatomy. Common 3D image modalities - CT, MR imaging, positron emission tomography (PET) - apart from greatly assisting in establishing diagnosis and organizing pre-operative/post-operative activities, can be conveniently utilized during surgery as well. However, their major drawback is that, being static, they do not completely reflect the surgical situation.
On the other hand, as seen in the description of fluoroscopic systems, it is mostly 2D images that are taken intra-operatively, because of timing, irradiation-related, and technological arguments. Yet, 2D images lack significant information that is present in the 3D modalities.
Ideally, one can recover the advantages of 3D data by aligning the intra-operative 2D images with pre-operative volumes ("3D roadmap"). To achieve this goal, it is necessary to determine their relative position (translational information) and orientation (angular information). The procedure that identifies a geometrical transformation able to align two datasets (*i.e.*, to locate one of them in the coordinate system of the other) is called registration[10] [15].
3D roadmaps are primarily suited for complex fluoroscopic surgery, such as branched aortic interventions. 3D image views provide continuous visualization of the origin of the side vessels for catheterizations, thus reducing the number of DSA images required for soft tissue visualization [16].
Available registration algorithms can be frame based, landmark based, surface based, or voxel based. Stereotactic (*i.e.*, frame-based) registration is accurate, but not practical outside the brain. Landmark-based methods use either external-point or anatomical point landmarks, and their accuracy is influenced by skin tissue and organ motion. Surface-based registration makes use of surface-segmentation algorithms, and is prone to errors when the surfaces are not easily identified. Conversely, the accuracy of voxel-based registration methods is not limited by segmentation errors.
For the specific case of fusing CT and fluoroscopic images, the primary focus is on registering bony structures, which are best visualized by both techniques. The characterization of the rigid movement of bones implies the tracking of six degrees of freedom, even though higher-dimensional transformations are needed to align finer details, such as soft tissues.
A key challenge consists of introducing an appropriate way to compare input images that are of different dimensionalities. The most common approach is to simulate one of the modalities given the other dataset and the current transformation estimate,

[10] When only translations and rotations of the datasets are taken into account, with no added deformation, the registration process is called "rigid". In clinical practice, the use of rigid-body models has proven successful in many applications, particularly when the anatomical structures of interests are bony landmarks such as the spine, or are surrounded by a rigid enclosing structure such as the brain.

so that the images can be compared in the same space. Then the transformation estimate is updated to maximize an alignment score according to some similarity function.
The reconstruction of 3D volumes from 2D images requires a number of projection acquisitions and large computation time, therefore simulating 2D images from 3D volumes is often preferred. Simulated projection images, whose construction usually implies the Monte Carlo modeling[11] of X-ray acquisitions, are named digitally reconstructed radiographs (DRRs). DRRs are formed by casting rays through the imaged 3D volume and summing up the attenuation coefficients of each voxel along the rays.

2.3.2.1 Transcatheter aortic valve implantation

A dramatic improvement in the non-invasive treatment of aortic stenosis in high-risk patients has been emerging since the introduction of transcatheter aortic valve implantation (TAVI) into clinical practice [17].
In the case of TAVI, an objective difficulty exists in performing reliable 2D-3D registration due to the moving nature of the observed object. A possible solution is using intra-operative contrast-enhanced rotational angiography for guidance and navigation, which however requires the injection of a contrast agent that is potentially harmful to the patient, not to mention the absence of a standard protocol for cardiac RA acquisition.
For this reason, in early 2010s a nonlinear 3D-3D registration procedure has been introduced [18] between the pre-operative CT and the intra-operative non-contrast-enhanced RA data, which relies on an initial rigid-body registration for coarse alignment, followed by a deformable registration for fine alignment. This type of non-rigid registration technique still lacks the robustness required for clinical practice, although research in the field is in progress.

[11] Monte Carlo methods constitute a large family of computational algorithms relying on repeated random sampling to get numerical simulations of physical processes.

3

X-ray radiation issues in the HOR

3.1 Safety first!

As anticipated in the Introduction, one of the major concerns with the transition from the conventional OR to the HOR is the increased intraoperative X-ray load per intervention.
The "as low as reasonably achievable"(ALARA) concept represents a mandatory practice that adheres to the recommendation by international radiation-protection agencies [19,20] of keeping patient- and medical-staff doses to a minimum in order to address growing concerns about radiation-induced somatic and heritable mutations.
Recalling the traditional classification of injury risks into deterministic and stochastic, the major deterministic hazards in a HOR are radiation-induced skin lesions (for patients) and eye lesions (for surgeons) [2–4]. For example, the (linear) deterministic dose threshold for the skin is 2 Gy, immediately above which a transient erythema may be detected [21] (Fig. 3.1).
On the other hand, the occurrence of stochastic radiation effects increases with increasing dose (but not linearly), and the effect severity is independent of total dose.

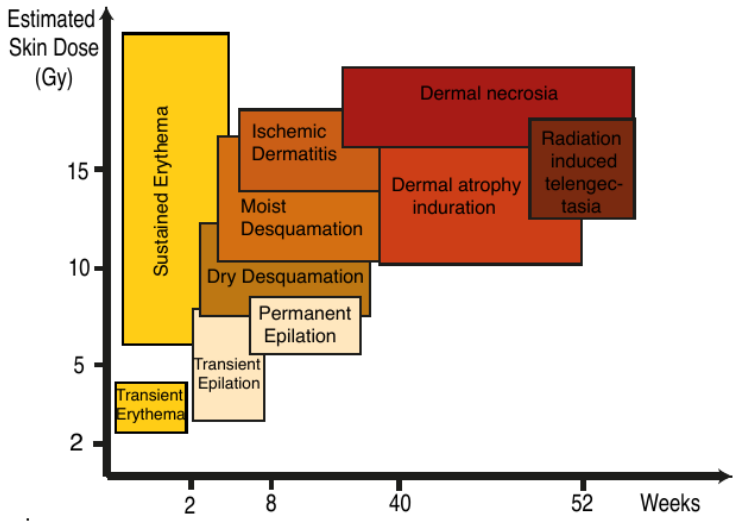

Figure 3.1: Overview of the relationship between entrance skin dose (ESD), time delay, and clinical manifestations. Adapted from [22].

3.2 Fluoroscopic dose metrics

Table 3.1 reports the major dose metrics usually employed within fluoroscopic procedures, as listed in the guidelines by the International Atomic Energy Agency (IAEA) [23].
The fluoroscopy time (FT), also known as the exposure time, is the most commonly reported metric, and includes the cumulative irradiation time during an imaging or interventional procedure. FT can be used as a rough dose overview, being the easiest metric to be interpreted; however, a reliable assessment of risks to the patients requires a focus on actual dose metrics, dose rates, and absorbed doses.
The kerma area product (KAP) is a measure of the total radiation energy entering the patient, and is obtained by integration of the air kerma[1] $K(x, y)$ over the X-ray beam cross-sectional area (or simply the product of the irradiated area surface by the absorbed radiation dose). It has the useful property of being approximately invariant with distance from the X-ray tube focus (when interactions in air and extrafocal radiation can be neglected), and represents a good indicator of stochastic risk (correlating with both patient and medical-staff doses). Yet, KAP is not an ideal[2] indicator of deterministic risk.
KAP can be measured by means of a KAP meter, based on a transparent ionization chamber mounted in the X-ray tube assembly.
The cumulative air kerma[3] (CAK) is, by definition, the air kerma accumulated at the patient skin at the international reference point[4] (IRP), and represents an indirect dose parameter to estimate deterministic skin risks to the patient.
The United States Food and Drug Administration (FDA) requires that any fluoroscope manufactured after June 2006 display the cumulative air kerma at either the IRP or a different point that is "deemed by the manufacturer to represent the intersection of the X-ray beam entrance surface and the patient skin" [26].
During surgery, CAK is spread over both operative time and space (from the abdominal to thoracic side and from anterior-posterior to lateral imaging).
This causes CAK to overestimate[5] the actual skin dose [27].
On the other hand, the peak skin dose (PSD) is a better predictor of the actual deterministic risk. Indeed, PSD is a direct risk estimator of radiation-induced skin disease, even though its measurement requires additional equipment, such as

[1] $K(x, y)$ is defined as the kinetic energy released per unit mass when an X-ray beam is traveling through air, and is expressed in Gy.

[2] A large dose delivered to a small skin area can yield the same KAP as a small dose delivered to a large skin area.

[3] The International Electrotechnical Commission (IEC) introduced the concept of cumulative air kerma in 2000 [25].

[4] For fluoroscopic systems, the IRP is located along the central line between the beam source and detector, 15 cm from the isocenter toward the focal spot [23] (Fig. 3.2). Thus, the IRP is fixed independently of the C-arm rotation, operating-table height, or table movements.
In addition, it does not include tissue backscatter.

[5] That's why, in spite of the above-mentioned 2-Gy threshold for deterministic risk for radiation-induced skin disease, a sentinel threshold of 5 Gy is set for CAK.

Table 3.1: Overview of dose metrics commonly used in fluoroscopy. EF, KAP, CAK, and PSD thresholds for patients are reported in [5] and ICRP Publication 85 [21], and represent recommended doses above which patients are eligible for follow-up on radiation-induced skin injury. The follow-up ED threshold for surgeons (eye lens) has been issued by IAEA in 2014 [24], following 2011 recommendations by the ICRP.

Dose metric	Explanation	Predictor for	Backscatter radiation	Unit	Recommended thresholds
Fluoroscopy time (FT)	Total irradiation time	Overall time (not dose)	NO	min	60 min (for patients)
Dose Area Product (DAP) or Kerma Area Product (KAP)	Total X-ray energy leaving the X-ray tube	Stochastic risk	NO	Gy cm^2	500 Gy cm^2 (for patients)
Cumulative Air Kerma (CAK)	Approximation of the total radiation dose to the patient skin	Deterministic risk	NO	Gy	5 Gy (for patients)
Peak Skin Dose (PSD)	Highest dose at any point of the patient skin	Deterministic risk	YES	Gy	3 Gy (for patients)
Effective Dose (ED)	Effective dose received by the patient or staff	Stochastic risk	YES	mSv	20 $\frac{mSv}{yr}$ (for surgeons)

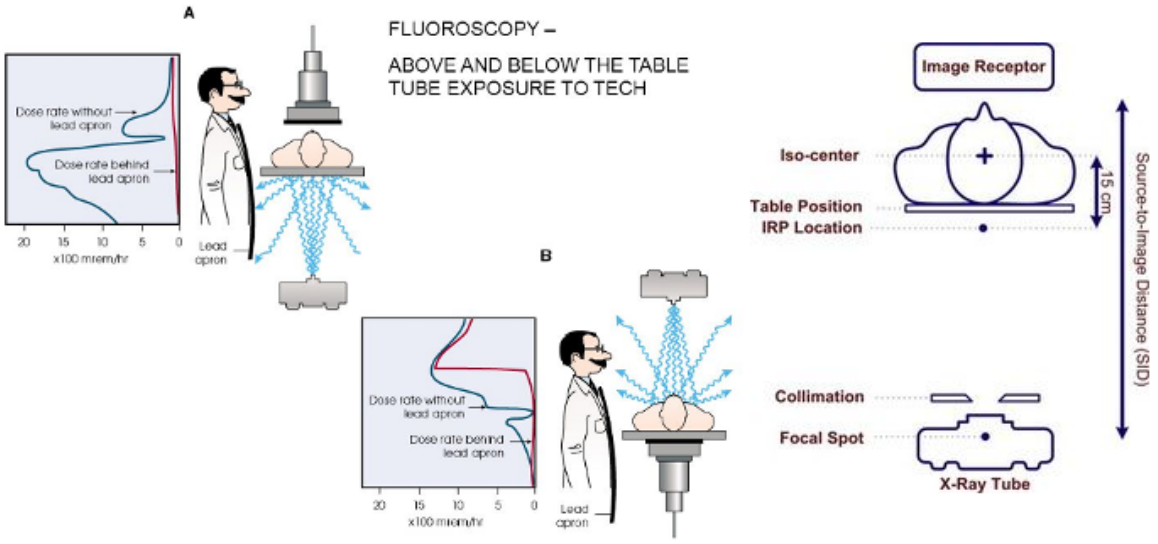

Figure 3.2: Position of the IRP in a C-arm system according to IAEA definitions [23] (right). Notice how the recommended position for the X-ray tube is *under* the patient, in order to minimize the dose rate to the head of the operator due to radiation (Compton) scattered by the patient (left). Adapted from Mosby, Inc. (2003).

radiochromic films[6] that must be positioned under the patient and analyzed by dedicated software.
PSD values are not displayed on the internal HOR monitor in real time during procedures. Nevertheless a linear relationship between PSD and CAK is often observed. This occurrence has an immediate clinical application, allowing operators to estimate PSD during surgery and apply corrective actions (*i.e.*, modifying the gantry angulation, table position, or collimation) to avoid skin injuries.
Finally, KAP can be utilized to retrieve the effective dose (ED) by calculation (ED= $C*$KAP). In this case the Sv is used as unit (instead of Gy), since one has to take into account that the absorbed dose must be corrected by organ- and radiation-type weighting factors[7] (C $[\frac{mSv}{Gy\ cm^2}]$) [23].
EDs from many medical procedures have been estimated using phantom measurements, Monte Carlo calculations and/or combinations of both.
Several secondary predictors of dose risk exist, which are suitably summarized in

[6] A radiochromic dosimeter is a film containing a dye, which polymerizes and changes color when exposed to ionizing radiation.
The resulting optical density can be read using a laser+photodiode sytem or a digitizer.
Radiochromic films are best suited for real-time personal dose monitoring because of their large dynamic range (10^2-10^6 Gy), insensitivity to visible light, no need for chemical processing, nearly flat angular response, intrinsic robustness.

[7] The Gy is the actual physical dose, corresponding to 1 $\frac{J}{kg}$. Yet, the effect of the radiation dose on the body changes with radiation type and affected tissue. For this reason, one defines the equivalent dose H_T (which multiplies the physical dose in Gy by a radiation-dependent factor: $H_T = \sum_R w_R D_{T,R}$) and the effective dose E (which multiplies the equivalent dose by a tissue-dependent factor: E= $\sum_T w_T H_T$), both quantified in Sv.

Table 3.2: Overview of secondary predictors of dose risk for the patient and operator during a fluoroscopic procedure, according to the three major factors subtended by the ALARA principle: distance, time, shielding. The ClarityIQ technology mentioned in the list is a new image-processing technology for Allura fixed C arms (Philips Healthcare), that is, an integrated image noise-reduction system that does not require any additional radiographic operating step to reduce the radiation dose while retaining image quality [28].

Absorbed dose	Increasing dose risk	Decreasing dose risk
Patient	Lateral imaging Magnification Overlapping fields Obesity Young age (< 60 yr) Multiple fluoroscopic procedures Aortic neck angulation ($> 60°$)	Use of collimation and wedges Pulsed scopy with minimal frame rate 3D imaging in complex procedures Dose-reduction technologies (*e.g*, Allura ClarityIQ)
Operator	Working on both sides of the table Lateral imaging DSA imaging Brachial access site	Operator-controlled imaging Ceiling-mounted lead shielding Sterile lead absorbing drapes Real-time Dose tracking system Table lead flaps X-ray transparent table X-ray grids Maximizing distance from the beam source Lead apron, thyroid shielding, lead glasses Operator Awareness

Figure 3.3: Members of medical staff starting a fluoroscopic procedure at Campus Bio-Medico University of Rome, Italy, in Feb 2018. The picture - taken through the shielded window of the control room - highlights the application of the ALARA principle, with maximization of distance (notice the secondary operator sitting behind a lead-glass shield at the edge of the room), time, and shielding (notice the usage of lead aprons, thyroid collars, table with lead flaps, lead-glass shielding, etc.).

Table 3.2 and are consistent with a typical fluoroscopic manouver as the one depicted in Fig. 3.3.
It is worth noticing here that, according to safety standards issued by IAEA in 2014 [24], the equivalent dose limit for the eye lens, in the case of occupational exposure in planned exposure situations[8], must be reduced from 150 mSv per year to 20 mSv per year averaged over defined periods of 5 years, with no annual dose in a single year exceeding 50 mSv.
This reduction in the dose limit for the eye lens has followed the recommendation of the International Commission on Radiological Protection (ICRP) in its statement on tissue reactions of Apr 21^{st}, 2011, and corresponds to a threshold of 0.5 Gy.
From this point of view, the transition from the mobile C arm to a HOR with fixed C arm can be challenging, provided that image quality and radiation dose are competing.

[8]No specific limit has been set for the eye lens in the case of members of the general public.

4

An experimental case from the literature

Although HORs are better equipped with radiation-shielding protection gear compared to standard ORs accommodating mobile C arms, members of the medical staff working in a HOR are at risk of absorbing higher radiation doses, due to higher exposure rates of fixed C arms when not used adequately [29].
The effective cumulative radiation dose absorbed by the staff is multifold and not constant, since it depends on the exposed radiation dose by the system, the amount of scattered dose from the patient, the dose settings of the X-ray system, the FT, personal shielding, and distance from the X-ray source. Indeed, even when KAP values are low, members of the personnel situated closer to patients during fluoroscopy could receive high occupational doses, unlike those (nurses, technicians) who are further away [30].
In spite of what said above, only a few experimental investigations have been performed so far in order to assess the radiation exposure to the entire operating team. The study presented in this chapter [31] is a recent quantitative characterization of occupational exposure (and also patient doses) in the first year of use of a HOR opened at the Hospital Clínico Universitario de Valladolid (Spain) to host vascular surgery.

4.1 The study by Andrés et al.

The instrumentation taken into account in the study is a multi-axis robotic X-ray imaging system with flat panel detector (Siemens Artis Zeego C arm by Siemens Healthcare), mounting an X-ray tube that spans the [40,125] kV range, and a KAP measurement chamber.
The tube potential and current are automatically adjusted under automatic exposure-rate control[1] (AERC).

[1] AERC is a feedback-type system that monitors the output of the image receptor and then adjusts the X-ray tube output based on an optimization algorithm, in an attempt to achieve a fixed level of image quality by modulation of the tube current (mA) and tube potential (kV).

For example, if a posterior-anterior view is being used and then the C-arm gantry is repositioned to perform a lateral view, the tube output will increase due to the increase in tissue thickness travelled through by the beam before reaching the image receptor.

When using AERC, it is important to ensure that nothing unnecessary is left in the field of view, as this provides additional beam attenuation, causing the X-ray source output to be automatically increased in an attempt to maintain image quality. This is especially true of dense or metallic

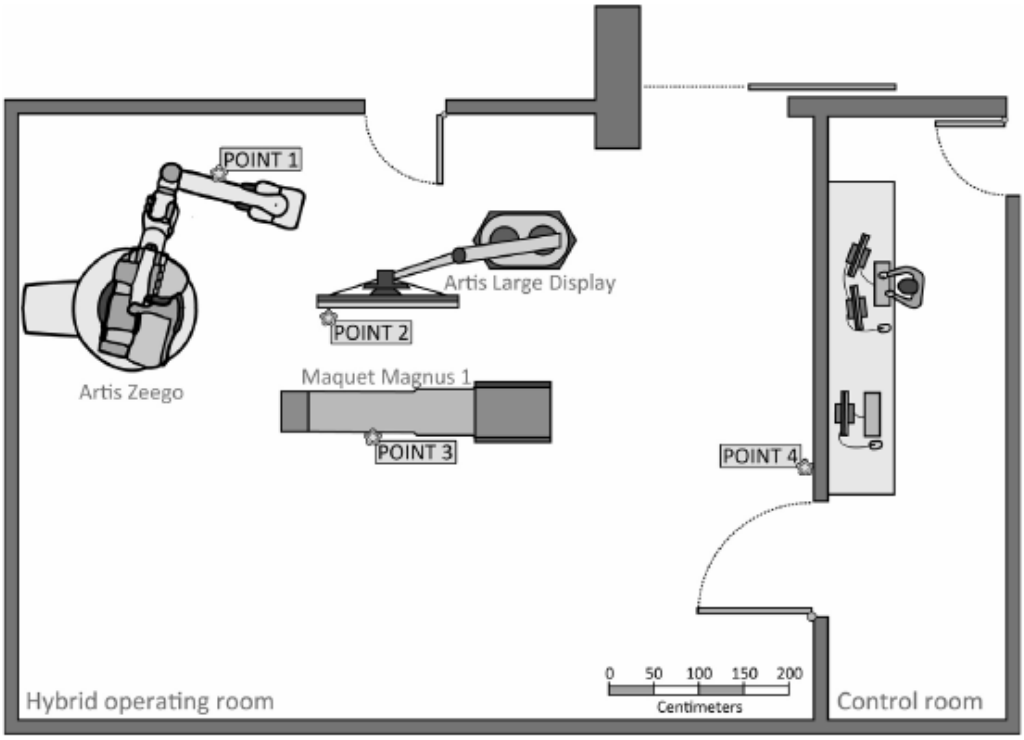

Figure 4.1: Schematic map of the investigated HOR at the Hospital Clínico Universitario de Valladolid (Spain), along with the location of the four ambient dose-equivalent measurement points. Tough no mention of the room perimetral shielding appears in the article, a 2-3 mm Pb lining can be reasonably presumed. The control room (with shielded doors and window) is appropriately separated from the interventional area. Reprinted from [31].

The HOR, whose map is reported in Fig. 4.1, accommodates two movable ceiling-mounted lead-glass shields (0.5-mm Pb equivalent).
All members of the HOR staff are requested to wear lead aprons (at least 0.25-mm Pb equivalent) and thyroid collars during interventional activities.
The study included 260 procedures (mainly angioplasty) over one year, with irradiation time $\geq$ 30 s and monitoring of FT, KAP, CAK, and PSD values both in scopy- and graphy mode[2].

items, such as lead aprons, which tend to attenuate X rays very effectively.

[2]The scopy mode implies low-dose, pulsed-emission, real-time imaging. The graphy mode aims to the digital recording of static, high-quality radiographic images, against the administration of higher radiation doses.

Table 4.1: Monthly ambient dose rate obtained in the 4 control points of the HOR. Adapted from [31].

Control point	Average $\left[\frac{mGy}{month}\right]$	Maximum $\left[\frac{mGy}{month}\right]$
Point 1 (C arm)	5.3 ± 0.8	6.7
Point 2 (Internal computer monitor)	0.8 ± 0.1	1.2
Point 3 (Internal control panel)	3.2 ± 1.1	6.7
Point 4 (Inner face of leaded glass)	≤ 0.1	0.1

The interventional area was monitored (on a monthly basis) by LiF:Mg TLD dosimeters[3] in order to assess the ambient dose equivalent[4] $H^*(10)$ (bottom threshold: 0.1 mSv) at four strategic points (Fig. 4.1): on the C arm, 1 m away from the isocenter (point 1); on the upper bracket of the internal computer monitor (point 2); on the system control panel located on the left side of the patient couch (point 3); and on the inner face of the leaded glass of the operator control zone (point 4).
Results of ambient monitoring are reported in Table 4.1.
The dependence of the ambient dose rate on distance from the patient is clear. The highest value is obtained at the measuring point nearest to the isocenter (on the C arm, point 1). Progressively lower dose equivalents are found at the control panel inside the room (point 3), which is usually anchored to the patient couch, and at the internal display (point 2), whose position is always relatively away from the patient. At the inner face of the leaded glass of the control room (point 4), the reading is below the TLD detection limit.
Each member of the medical staff was monitored (on a monthly basis) by a TLD badge worn under the lead apron at the chest height. In the first twelve surgical procedures, also a direct-reading Mk2+ electronic personal dosimeter (placed at chest high over the lead apron[5]) was used to recover the personal deep dose equivalent $H_p(10)$ and skin dose equivalent[6] $H_p(0.07)$ received by the head physician (most

[3]Thermoluminescent dosimeters (TLDs) are solid-state devices that work on the basis of charge-storage principle.

Often made of alkali/alkaline-earth metal fluorides, they include impurities in the crystal lattice in order to produce electron trap states ("luminescence centers") at different depths (*i.e.*, energies) in the forbidden region separating valence band from conduction band. They do not represent real-time dosimeters, which need to be "read"by heating after exposition. Indeed, heating causes the excited trapped electrons to drop back to their ground state, releasing photons of energies that correspond to the energy difference between trap states and ground state. The result is a counts-vs-temperature "glow curve", which returns dose estimates by peak integration.

[4]The ambient dose equivalent $H^*(10)$ is the equivalent dose at a point in a radiation field that would be produced by the corresponding expanded and aligned field in a 30-cm-diameter sphere of unit-density tissue (ICRU sphere) at a depth of 10 mm on the radius vector opposing the direction of the aligned field [33].

[5] Generally, a single dosimeter worn under a lead apron will yield a reasonable estimate of the effective dose. However, in catheterization laboratories, it is recommended that the physician wear two monitors: one under the lead apron and one outside the lead shield (preferably at the collar) [32].

[6]The personal dose equivalent $H_p(d)$ is the equivalent dose in soft tissue (ICRU sphere) below a specified point on the body at an appropriate depth d [33].

d is expressed in mm. For superficial organs, depths of 0.07 mm for skin and 3 mm for the lens

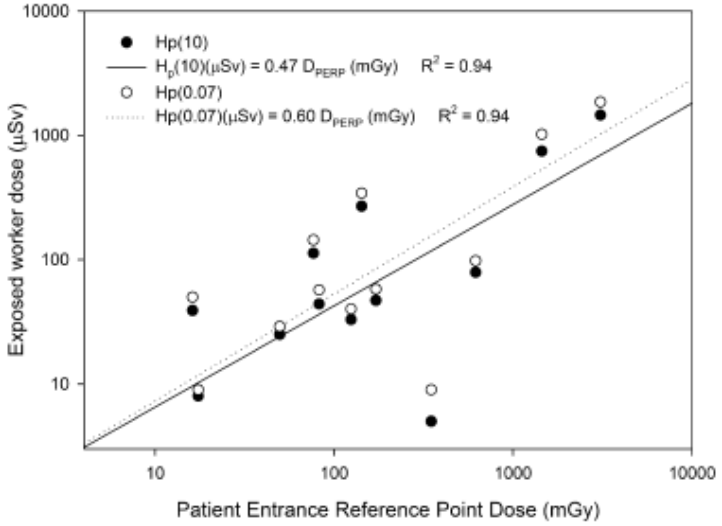

Figure 4.2: $H_p(10)$ and $H_p(0.07)$ for the most exposed worker as a function of CAK. Reprinted from [31].

exposed worker).
Such dose equivalents (per procedure) are reported in Table 4.2.
Individual monitoring is consistent with area-monitoring values, and shows a linear relationship between $H_p(10)$, $H_p(0.07)$ and CAK (Fig. 4.2).
In particular, the staff effective dose is lower than the dose registered by the direct reading dosimeter worn outside the apron, and may be estimated by dividing the dosimeter reading by a factor of 6, according to calculation methods recommended by the National Council on Radiation Protection (NCRP) [34, 35].
The results of patient dosimetry can be found in Table 4.3. The monitoring of the patient dose via KAP revealed a median per procedure of 26.0 Gy cm^2, that is, a value on the same order of magnitude as other endovascular dose studies performed in HORs [36], which can be used to establish reference levels[7] for interventional procedures in hybrid theaters.
It appears clear that patient exposure strongly depends on the irradiation mode, provided that approximately 65% of the PSD is due to the contribution of graphy, despite it represents less than 5% of the total irradiation time in the HOR.

of the eye are employed. For deep organs, a depth of 10 mm is frequently used.

Operative definitions reported in [33] have been transferred to the Italian Legislative Decree 230/95, modified by the Legislative Decree 241/00.

[7]Diagnostic reference levels (DRLs) have been introduced by ICRP in 1996 [37] and established by the European Directive 2013/59/Euratom [38] as an instrument for the optimization of patient exposure during diagnostic procedures involving ionizing radiation.

DRLs are not to be applied to the single patient or used as dose limits. Rather they represent an essential tool to select those radiological practices that need corrections in order to reduce doses administered to patients [39].

Table 4.2: Deep dose equivalent and skin dose equivalent received by the head physician per procedure. Adapted from [31].

	$\mathbf{H_p(10)}$ **[mSv]**	$\mathbf{H_p(0.07)}$ **[mSv]**
Average	0.24 ± 0.25	0.31 ± 0.32
Maximum	1.46	1.85

Table 4.3: Patient dose metrics and their dependence on irradiation mode. Adapted from [31].

Metric	Irradiation mode	Average	Median	Maximum
FT [hh:mm:ss]	Scopy	00:18:19	00:13:35	02:20:33
	Graphy	00:00:56	00:00:40	00:03:56
KAP [Gy cm^2]	Total	66.9	26.0	2099
	Scopy	21.2	5.4	1218
	Graphy	45.7	16.4	881
KAC [Gy]	Total	0.41	0.11	9.31
	Scopy	0.14	0.03	5.42
	Graphy	0.27	0.07	3.97
PSD [Gy]	Total	0.23	0.08	2.88

5

Conclusions

The study by Andrés *et al.* is a quantitative example of the feasibility of safe work in a HOR from the point of view of protection from ionizing radiation.
Thanks to surgical-team rotations, effective doses administered to the medical staff were found markedly lower than the safety limit established by the ICRP for workers[1] (20 mSv per year) and incorporated into the (modified) Italian Legislative Decree 230/95. On the other hand, apart from one single patient receiving a PSD of 2.9 Gy due to a complex endoprosthesys (and being subject to a 2-week follow-up), the median PSD was found roughly 20 times lower than the threshold dose for deterministic skin effects to patients, 2 Gy, set by ICRP [21].
The future of radiation exposure in the HOR lies in innovations focused on dose-reduction software and hardware.
For sure, after vascular surgery, other specialties, such as neurosurgery, traumatology, and oncology, will find their way into the HOR and will incorporate the use of advanced X-ray imaging and 3D imaging.

[1] A-category workers in Italy.

Bibliography

[1] Portou, M.J., Browne, T.F., and Prionidis, I. (2011). *The vascular hybrid operating theatre: The Broomfield Hospital experience*. RAD Magazine **37**(437), 29-31.

[2] Sanchez, R., and others (2010). *Staff Radiation Doses in a Real-Time Display Inside the Angiography Room*. Cardiovasc. Intervent. Radiol. **33**(6), 1210-1214.

[3] Howells, P., and others (2012). *Risk of Radiation Exposure during Endovascular Aortic Repair*. Eur. J. Vasc. Endovasc. Surg. **43**, 393-397.

[4] Monastiriotis, S., Comito, M., and Labropoulos N. (2015). *Radiation exposure in endovascular repair of abdominal and thoracic aortic aneurysms*. J. Vasc. Surg. **62**(3), 753-761.

[5] Stecker, M.S., and others (2009). *Guidelines for patient radiation dose management*. J. Vasc. Interv. Radiol. **20**, S263-S273.

[6] Miller, D.L., and others (2010). *Occupational Radiation Protection in Interventional Radiology: A Joint Guideline of the Cardiovascular and Interventional Radiology Society of Europe and the Society of Interventional Radiology*. Cardiovasc. Intervent. Radiol. **33**, 230-239.

[7] Jolesz, F.A. Ed. *Intraoperative Imaging and Image-Guided Therapy*. Springer, 2014.

[8] Buzug, T.M. *Computed Tomography: From Photon Statistics to Modern Cone-Beam CT*. Springer, 2008.

[9] Hill, D.G. *Electron Beam CT of the Heart*. In Schoepf U.J. Ed., *CT of the Heart*, Totowa, N.J.: Humana Press, 2005.

[10] Lerman, L.O., and others (1999). *The development of x-ray imaging to study renal function*. Kidney International **55**(2), 400-416.

[11] Bushberg, J.T., and others. *The essential physics of medical imaging*. Lippincott, Williams and Wilkins, Philadelphia, 2002.

[12] Kalender, W.A., and others (1989). *Single-breath-hold spiral volumetric CT by continuous patient translation and scanner rotation*. Radiology **173**, 414.

[13] Kottal, S. *Three-Dimensional Basics: CT vs. CBCT*. March 3rd, 2014. <https://carestreamdentalblogdotcom1.wordpress.com/2014/01/03/three-dimensional-basics-ct-vs-cbct/>

[14] Seibert, J.A. (2006). *Flat-panel detectors: how much better are they?*. Pediatr. Radiol. **36**(2), 173-181.

[15] Zoellei, L., and others. *2D-3D Rigid Registration of X-Ray Fluoroscopy and CT Images Using Mutual Information and Sparsely Sampled Histogram Estimators*. In CVRP 2001 Conference Proceedings, 2001.

[16] Fukuda, T., and others (2013). *Evaluation of automated 2D-3D image overlay system utilizing subtraction of bone marrow image for EVAR: feasibility study.* Eur. J. Vasc. Endovasc. Surg. **46**(1), 75-81.

[17] Hamm, C.W., and others (2016). *The future of transcatheter aortic valve implantation.* European Heart Journal **37**, 803-810.

[18] Lu, Y., and others. *Registration of Pre-operative CT and Non-Contrast-Enhanced C-Arm CT: An Application to Trans-Catheter Aortic Valve Implantation (TAVI).* In ACCV 2012 Conference Proceedings, 2012.

[19] *ICRP Publication 60 - 1990 Recommendations of the International Commission on Radiological Protection.* Annals of the ICRP, 1991.

[20] *Standards for protection against radiation.* Nuclear Regulatory Commission. Final rule. Federal Register **56**, 23360-23474, 1991.

[21] *ICRP Publication 85 - Avoidance of radiation injuries from medical interventional procedures.* Annals of the ICRP, 2000.

[22] Hertault, A., and others (2015). *Minimizing Radiation Exposure During Endovascular Procedures: Basic Knowledge, Literature Review, and Reporting Standards.* Eur. J. Vasc. Endovasc. Surg. **50**, 21-36.

[23] *IAEA Safety Report no. 59 - Establishing Guidance Levels in X Ray Guided Medical Interventional Procedures: A Pilot Study.* IAEA Safety Report Series, 2009.

[24] *IAEA Safety Standard no. GSR Part 3 - Radiation Protection and Safety of Radiation Sources: International Basic Safety Standards.* IAEA Safety Standards Series, 2014.

[25] *IEC Report 60601 - Medical Electrical Equipment - Part 2-43: Particular Requirements for the Safety of X-ray Equipment for Interventional Procedures.* IEC, Geneva, 2000.

[26] *United States Food and Drug Administration. Code of Federal Regulations, 21CFR1020.32(XX), Part 1020 - Performance standards for ionizing radiation emitting product.* Silver Springs, MD: FDA, 2002.

[27] Geise, R.A., and others (1999). *Radiation dose in interventional fluoroscopic procedures.* Appl. Radiat. Isot. **50**, 173–184.

[28] de Ruiter, Q.M., and others (2016). *AlluraClarity Radiation Dose-Reduction Technology in the Hybrid Operating Room During Endovascular Aneurysm Repair* J. Endovasc. Ther. **23**(1), 130-138.

[29] Albayati, M.A., and others (2015). *Angulation of the C-arm during complex endovascular aortic procedures increases radiation exposure to the head.* Eur. J. Vasc. Endovasc. Surg. **49**(4), 396-402.

[30] Sanchez, R.M., and others (2016). *Occupational eye lens doses in interventional cardiology. A multicentric study.* J. Radiol. Prot. **36**(1), 133-143.

[31] Andrés, C., and others (2017). *Patient doses and occupational exposure in a hybrid operating room.* Physica Medica **37**, 37-42.

[32] American College of Cardiology: ACC expert consensus document (1998). *Radiation safety in the practice of cardiology.* J. Am. Coll. Cardiol. **31**, 892-913.

[33] *ICRU Report no. 51 - Quantities and Units in Radiation Protection Dosimetry.* ICRU Report Series, 1993.

[34] *NCRP Report no. 122 - Use of personal monitors to estimate effective dose equivalent and effective dose to workers for external exposure to low-LET radiation.* NCRP Report Series, 1995.

[35] Chida, K., and others (2009). *Effect of Radiation Monitoring Method and Formula Differences on Estimated Physician Dose during Percutaneous Coronary Intervention.* Acta Radiol. **2**, 170-173.

[36] Segal, E., and others (2013). *Patient radiation exposure during percutaneous endovascular revascularization of the lower extremity.* J. Vasc. Surg. **58**(6), 1556-1562.

[37] *ICRP Publication 73 - Radiological Protection and Safety in Medicine.* Annals of the ICRP, 1996.

[38] Council Directive 2013/59/EURATOM. Official Journal of the European Union **L13**, 2014.

[39] Padovani, R., and others. *Rapporto Istisan 17/33 - Livelli Diagnostici di Riferimento Nazionali per la Radiologia Diagnostica e Interventistica.* Istituto Superiore di Sanità, 2017.

[40] Tang, K., and others (2012). *Effect of Low Tube Voltage on Image Quality, Radiation Dose, and Low-Contrast Detectability at Abdominal Multidetector CT: Phantom Study.* J. Biomed. Biotechnol. **2012**, 130169.

A

The X-ray tube

In electron-impact X-ray sources (X-ray vacuum tubes), the emitted radiation - generated by the deceleration (*bremsstrahlung*) of fast electrons entering a solid metal anode and by the characteristic emission of the anode material - consists of e.m. waves spanning the $[6 \cdot 10^{-12}, 6 \cdot 10^{-10}]$-m wavelength range and the $[5 \cdot 10^{17}, 5 \cdot 10^{19}]$-Hz frequency range. The radiation energy depends on the electron velocity, which in turn depends on the acceleration voltage between the cathode and anode (Fig. A.1).
One of the major applications of such an indirect[1] and controllable ionizing radiation is in medical diagnostics (with voltages between 25 and 150 kV).
An electron cloud is "boiled off"from a cathode filament embedded in a heating circuit (thermoionic emission), and accelerated by the acceleration voltage before hitting a small focal point[2] on the anode. The corresponding emission current density, j_e, is basically a function of temperature, and is described by the Richardson-Dushman equation[3].
The spectrum of the radiation emitted by an X-ray tube (Fig. A.2) is typically shaped as a smooth, continuous[4] curve (due to *bremsstrahlung*) superimposed by a set of sharp spikes, which correspond to characteristic atomic K-shell lines for the anode metal[5].
The conversion efficiency from kinetic electron energy to *bremsstrahlung* energy can be described by

[1] X rays - like neutrons, and unlike α- and β emissions - are indirectly ionizing in the sense that they cede their energy after a few interactions with the medium, then generating electrons which are directly responsible for ionization phenomena.

[2] The focal-point size is on the order of the mm.

To produce a small electron focus on the anode - which is important to preserve image quality in imaging systems - electron trajectories must be controlled by electron optics.

[3] According to the Richardson-Dushman equation, j_e can be expressed as

$$j_e = \frac{4\pi m_e k_B^2 e}{h^3} T^2 e^{\frac{-\phi}{k_B T}}, \tag{A.1}$$

where m_e is the electron mass, e is the electron charge, k_B is the Boltzmann constant, h is the Planck constant, T is the absolute temperature, and ϕ is the work function (defined as the difference between the binding energy and the Fermi energy edge).

[4] Free electrons are unbound, thus their energy cannot be quantized.

[5] For elements with low atomic numbers, this characteristic emission is dominated by a competing Auger process.

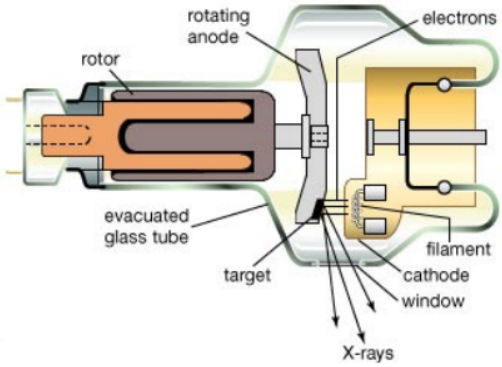

Figure A.1: Scheme of a rotating-anode X-ray tube, usually enclosed in a Pb cuff to increase protection against escape radiation. Reprinted from Merriam-Webster, Inc. (2006).

$$\eta = KZU_a, \tag{A.2}$$

where K is the Kramers constant (equal to $9.2{\cdot}10^{-7}$ kV^{-1}), Z is the atomic number of the anode material, and U_a is the acceleration voltage (in kV).
At the typical voltages used in diagnostics, Eq. A.2 returns a very modest $\eta \sim 0.01$, which means that around 99% of the kinetic energy is transferred to the lattice, heating up the anode. In other words, X-ray tubes have serious heat problems.
A significant step forward in distributing the thermal load over the entire anode was represented by the introduction of the rotating anode in the late 1920s. In this configuration, the anode target material is rotated about the central axis, so that the energy of the electron beam is spread out over a circular line (focal line), rather than being concentrated at one single point (Fig. A.1). In modern tubes, a significant part of the heat (about 30%) is conducted via the bearing of the rotating anode, while the rest of the heat is transferred via radiation to the tube housing. In addition, the tube is usually oil-cooled.
Due to larger cross-sections, low-energy X rays are more strongly attenuated when passing through matter than their high-energy counterpart. This phenomenon has two important disadvantages: one is its impact on image quality, since such an attenuation shifts the polychromatic beam towards higher energies (beam hardening), thus generating artifacts in the reconstructed images [8]; the other is of radiological interest, because low-energy X rays, being almost totally absorbed by the body, increase the dose to the patient (and operator) with no contribution to imaging.
For this reason, apart from inherent filtration operated by the tube window, the X-ray tube generally mounts a few-mm flat metal filter, which cut low frequencies off (Fig. A.2, left).
When the tube current is kept constant and the acceleration voltage is increased, X-ray energy and number of photons gradually increase, together with the brightness of the image area and the administered dose (Fig. A.2, center). Conversely, the image contrast is reduced.

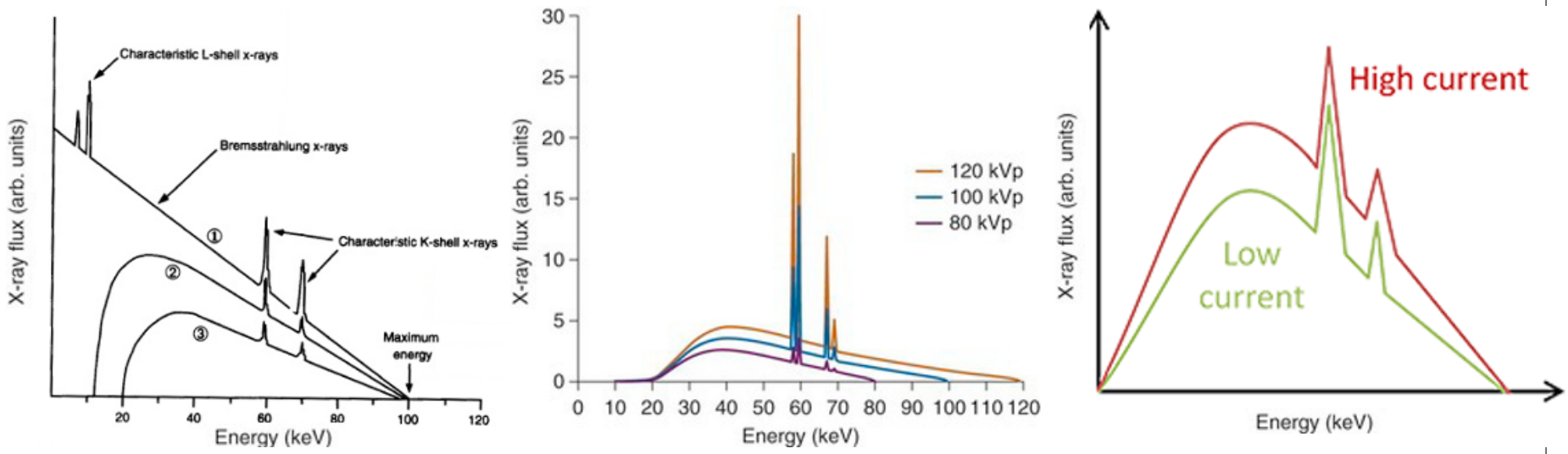

Figure A.2: Typical shape of a radiation spectrum from an X-ray tube, and its dependence on filtration (left), acceleration voltage (center), and tube current (right). Left: curve 1 = spectrum immediately out of the anode (no filtration), curve 2 = same spectrum after inherent filtration (through the window of tube housing), curve 3 = same spectrum after additional filtration. Center: change in quantity (vertical) and quality (horizontal) following change in acceleration voltage. Right: change in quantity following change in tube current.

When the acceleration voltage is kept constant and the tube current is increased, the number of photons of same energy within the scan grows (Fig. A.2, right), so enriching the gray scale of the resulting image, with gain in contrast-to-noise ratio (CNR), but dose as well [40].
It is to the operator the choice of voltage- and current values suitable to optimization of image quality and radiation protection.